Article

Journal of the Brazilian Chemical Society

https://dx.doi.org/10.21577/0103-5053.20240133

J. Braz. Chem. Soc. **2025**, *36*, 2, e-20240133, 1-10
©2025 Sociedade Brasileira de Química

Silver Electrodeposition in Amide-Based Low-Temperature Molten Salt and Its Surface-Enhanced Raman Scattering Effect

Cheng Y. Liu, *[*,a,b] **Chao Y. Jie,***[a] ***Dao Cao,***[a,b] ***Yu Liu,***[a,b] ***Feng Cui Li***[a,b] ***and Shu N. Gao***[a]

[a] *Henan University of Urban Construction, Pingdingshan 467036, China*

[b] *Henan Engineering Technology Research Center for Green Energy Development and Comprehensive Application, Pingdingshan 467036, China*

Silver film is commonly used to examine the structure and composition of molecules due to its surface-enhanced Raman scattering (SERS) effect. A simple method for preparing SERS silver films is proposed in this paper by electrodeposition in an amide-based liquid mixture (urea-acetamide-LiBr). The electrochemical behavior of silver in urea-acetamide-LiBr mixture was studied by cyclic voltammetry (CV) and chronoamperometry. It was found that the nucleation mechanism of silver shifts to instantaneous nucleation under diffusion control with increasing overpotential and temperature. The energy dispersive spectroscopy (EDS) and X-ray diffraction (XRD) investigations confirmed that the obtained deposits are pure silver. Scanning electron microscopy (SEM) analysis showed that the morphology of the silver deposits depends on the deposition potential and temperature. Rhodamine 6G was used as probe molecules for SERS experiments, showing that these new active substrates have high sensitivity to SERS response with high enhancement factors, of approximately 10^7, and enable Raman scattering even for diluted solutions.

Keywords: silver, urea-acetamide-LiBr, electrodeposition, SERS active

Introduction

Surface-enhanced Raman scattering (SERS) has been greatly emphasized and used as a powerful analytical technique in the directions of physics, chemistry, environmental protection, biology, new materials, medicine, and agriculture due to its unique fingerprint spectrum, rapid and nondestructive detection without sample pretreatment, and high detection sensitivity.[1,2]

In recent years, the preparation of SERS active substrates has been a hot spot in its research field.[3,4] The preparation of SERS substrate is always the most critical part, and its research progress has a profound impact on the application scope of SERS technology.[5,6] Mazur *et al.*[7] reported a quick one-step fabrication of efficient SERS substrates by a modified approach based on a silver-mirror reaction. The achieved detection level of a standard dye analyte was 10^{-13} mol L^{-1} rhodamine 6G (R6G).[7] Luo *et al.*[8] processed a new patterned SERS platform via femtosecond laser, achieving attomolar detection with an enhancement factor of 1.09×10^{14}. The relative standard deviation (RSD) was 11.7% at 10^{-14} mol L^{-1}.[8] Dzhagan *et al.*[9] developed an efficient SERS substrate by an original one-step synthesis of highly monodisperse SiO_2 spheres and deposition of the Ag layer. The substrates allowed easy detection of rhodamine 6G concentrations as low as 10^{-13} M. Coluccio *et al.*[10] obtained silver-based substrate fabrication using nanolithography and site-selective electroless deposition. This new active substrate exhibited high sensitivity to SERS response and enabled Raman scattering even for diluted solutions (10^{-20} mol L^{-1}) using rhodamine 6G as probe molecules.[10] Virga *et al.*[11] obtained the Ag nanoparticles by immersion plating of porous silicon samples in $AgNO_3$ aqueous solutions, controlling the morphology and the average particle sizes. Enhanced Raman activity of the substrates was tested using cyanine Cy3-H (Cy3) and R6G dyes as probe molecules, which was larger than 10. Yu *et al.*[12] proposed a novel hybrid hybrid superhydrophobic/-philic (SH/SHL) microporous SERS substrate. The optimized SERS sensor was capable of detecting rhodamine 6G at attomolar levels (10^{-17} mol L^{-1}) using analyte volumes as small as 5 µL, corresponding to an enhancement factor of 5.19×10^{13}.[12]

Compared to other materials, silver-based materials can provide a huge electromagnetic field contribution in the visible region and have a high surface plasma

---

*e-mail: liu_chy@126.com
Editor handled this article: Rodrigo A. A. Muñoz (Associate)

resonance effect and high SERS activity at a relatively low cost, so they are widely used in SERS substrates.[13,14] The electrodeposition is relatively simple, easy to operate, and easy to control. The prepared materials usually have high purity and stability, and large-area preparation of materials can be used to obtain bulk materials, which are suitable for large-scale mass production. By controlling the deposition rate and microscopic morphology through adjustments in current density and temperature during electrodeposition, materials with different microscopic morphologies and sizes can be prepared, , often meeting the requirements for optimal. Ibañez *et al.*[15] investigated the electrodeposition process of silver nanoparticles using UV-Vis spectroscopy and Raman spectroelectrochemistry to provide *in situ* information for the synthesis of silver nanoparticles by cyclic voltammetry. It was shown that the SERS effect strongly depends on the size and shape of the nanoparticles. Rivera *et al.*[16] synthesized large-area, high-purity, and highly surface roughened arrays of silver nanoplates by a simple electroplating/etching method, which were successfully applied in the detection of deoxiribonucleic acid (DNA), proteins, and viruses. Xia *et al.*[17] used a simple constant-current electrodeposition method with copper substrate to prepare high-density SERS substrates. The enhancement factor for the detection of R6G molecules was 2.0×10^5 with high-intensity SERS signal and a high reproducibility. The method has been successfully used for the preparation of different metal substrates, demonstrating the potential of the electrodeposition method for a wide range of applications in different fields.[17]

Amide-based low-temperature molten salts consisting of amides and one of alkali metal halides display low melting points, good solubility of metal chlorides, and high ionic conductivities.[18] Compared to ionic liquids, amide-based low-temperature molten salts have the following advantages: cheaper price, simpler synthetic process, higher solubility for many metal chlorides, and excellent stability at a greater temperature range.[19] Hence, amide-based molten salts are excellent media for metal and alloy electrochemical deposition. The electrodeposition of a series of metal-based alloys has been carried out in the amide-based salts. Liu *et al.*[20] studied the electrodeposition of Fe and Nd in acetamide-urea-NaBr-KBr. Nd-Fe can be induced co-deposition. At a potential of –1.25 V, the composition of the Nd-Fe film varied with the $\text{Nd}^{\text{III}}/\text{Fe}^{\text{II}}$ molar ratio, achieving a maximum Nd content of 60.4 wt.%. Nd-Fe film comprised nanoparticles with a size of about 100-200 nm.[20] They also investigated the electrodeposition of Co^{II} and $\text{Co}^{\text{II}} + \text{Sm}^{\text{III}}$ in urea-acetamide-NaBr. The reduction of Co^{II} is an irreversible process, and Sm^{III} cannot be reduced alone, but Sm-Co can be co-deposited by induced deposition. The mechanism may involve a polynuclear complex containing Co^{II} and Sm^{III}.[18] Wang *et al.*[21] prepared the Co-La alloy films by electrodeposition in urea-NaBr melt. The lanthanum was co-deposited by the inducement effect of cobalt to form Co-La alloy. The Co-La alloy film is suitable to be used as memory magnetic material. Li *et al.*[22] deposited the rare earth (RE)-3d transition metal (TM) films in low-temperature urea-acetamide-NaBr-KBr. It is reasonably suggested that the RE-induced co-deposition ability and efficiency were dominated by the electronegativity difference between RE and TM atoms.[22]

In the present work, the electrochemical reduction process and nucleation mechanism of silver ions are researched and the electrodeposits are characterized to get more insights into the electrochemical study of silver in the urea-acetamide-LiBr melt. The surface-enhanced Raman scattering effect was also conducted on the silver deposits obtained in this work.

Experimental

Acetamide (Sinopharm Chemical Reagent Co. Ltd., Shanghai, China, > 98.5%) and urea (Sinopharm Chemical Reagent Co. Ltd., Shanghai, China, > 99%) were dehydrated under vacuum at 333 and 353 K for more than 24 h, respectively. Anhydrous silver chloride (Sinopharm Chemical Reagent Co. Ltd., Shanghai, China, ≥ 99.5%), lithium halide (Alfa Aesar, Heysham, United Kingdom, ≥ 99%), and rhodamine 6G (Aladdin, Shanghai, China, ≥ 99%) were used as received.

The amide-based molten salt was prepared by stirring a mixture of urea, acetamide, and LiBr at 353 K until a homogeneous and colorless liquid formed with the following composition: 3.45 mol% urea, 5 mol% acetamide, and 1 mol% LiBr. A solution of AgCl in urea-acetamide-LiBr molten salt was prepared by adding 0.08 mol L^{-1} AgCl to the molten salt and stirring with a magnetic stir bar at 353 K until complete dissolution of AgCl. All the operations were carried out in an argon-filled glove box with the contents of water and oxygen below 0.1 ppm.

All the electrochemical experiments were processed with a three-electrode assembly using an AUTOLAB (Metrohm PGSTAT 30, Herisau, Switzerland) potentiostat/galvanostat controlled by GPES software. A tungsten wire (diameter (∅) = 1 mm, 0.157 cm^2) was used as an inert working electrode. A platinum wire (∅ = 1 mm) and a high-purity silver wire (∅ = 0.5 mm) were used as the counter electrode and *quasi*-reference electrode, respectively. All the electrodes were polished thoroughly with emery paper, and then cleaned with ethanol before the use.

The deposit samples were prepared by potentiostatic deposition on copper substrates (0.5 × 0.5 cm^2) at different potentials and temperatures for 2 h, and then washed in anhydrous ethanol to remove salt adhered to the cathode surface, and stored in the glove box before characterization. The surface morphology and chemical analysis of the electrodeposits were measured with scanning electron microscopy (SEM) combined with energy dispersive spectroscopy (EDS) (ZEISS-EVO18, Oberkochen, Germany), and the composition of the samples was analyzed by X-ray diffraction (XRD) (PANalytical MPDDY 2094, Almelo, Netherlands).

Rhodamine 6G (R6G) was chosen as the probe molecule to test the SERS effect of electrodeposited silver. The deposits were immersed in a 10^{-4} mol L^{-1} aqueous solution of R6G for 2.5 h, and then rinsed with deionized water to remove the chemical adsorption on silver substrates. The surface-enhanced Raman spectra were recorded at room temperature via a Raman spectrometer with the excitation light of a He-Ne laser at 633 nm wavelength (Horiba Jobin Yvon LabRAM HR 800, Paris, France).

Results and Discussion

Linear scan voltammetry (LSV) using a tungsten working electrode was performed in urea-acetamide-LiBr with a scan rate of 200 mV s^{-1} at 353 K (Figure 1a). The results show that the cathodic limit is −1.2 V, while the anodic limit 1.0 V (*vs.* Ag/Ag^+). The electrochemical window of blank urea-acetamide-LiBr is found to be ca. 2.2 V. No significant current is observed within this electrochemical window range, indicating that the reaction of impurities in the melt is negligible within this potential range.[18]

To investigate the electrochemical behavior of silver, cyclic voltammetry (CV) was carried out in urea-acetamide-LiBr containing AgCl (0.08 mol L^{-1}) at 353 K in the potential range of 0.70 V to –0.85 V (*vs.* Ag/Ag^+) with a scan rate of 200 mV s^{-1} at 353 K. The typical CV curve obtained in urea-acetamide-LiBr ILA is presented in Figure 1a. It shows only one cathodic process in the forward scan at about −0.50 V (*vs.* Ag/Ag^+). The reduction peak was associated with the electrodeposition of silver metal. The reverse anodic scan showed a crossover loop, suggesting a typical nucleation process. This indicates that the electrodeposition of Ag on the tungsten electrode requires an overpotential to initiate the nucleation and growth of Ag. The similar behavior was also reported in the literature.[23]

As shown in Figure 1b, the reduction and oxidation current densities increased significantly with increasing temperature, and the difference between the reduction peak potential and the oxidation peak potential became smaller, indicating that the reversibility of the electrode reaction was enhanced with increasing temperature. This relates to the migration of charges of electroactive substances in the electrolyte, where the substance transfer rate increases with rising temperature. Meantime, the cathodic peak potentials shift toward more negative potentials as the scan rate increases, and the difference between the cathodic and anodic peak potentials is significantly larger than the theoretical value expected for a reversible process (Figure 1c). This indicates that the reduction of Ag^I proceeds via a one-step irreversible charge transfer process.

For an irreversible electrochemical process, the charge transfer coefficient can be calculated according to equation 1:[24]

$$|E_p - E_{p/2}| = 1.857RT / \alpha n_\alpha F \quad (1)$$

where E_p and $E_{p/2}$ are the cathodic peak and half-peak potential, V; R and F is the gas constant (8.314 J K^{-1} mol^{-1}) and Faraday constant (96485 C mol^{-1}), respectively; T is the temperature (K); α is charge transfer coefficient; n_α is the number of exchanged electrons ($n_\alpha = 1$). According to equation 1 and data obtained from Figure 1, the average transfer coefficient can be calculated as 0.60.

Figure 1d shows a linear relationship between peak current density (j_p) *vs.* square root of scan rate ($\nu^{1/2}$). For an irreversible electrode reaction, the diffusion coefficient of Ag^I can be calculated according to equation 2:[24]

$$j_p = 0.4958nFc^0(\alpha n_\alpha F / RT)^{1/2}D^{1/2}\nu^{1/2} \quad (2)$$

where j_p is the cathodic peak current density (A cm^{-2}); c^0 is the initial concentration of electroactive species (mol cm^{-3}); D is the diffusion coefficient (cm^2 s^{-1}), v is the scan rate (V s^{-1}). Combining equation 2 with α and the slope of the line in Figure 1d, the diffusion coefficient of Ag^I was calculated to be 1.38×10^{-6} cm^2 s^{-1} at 353 K.

Chronoamperometric experiments were performed at the interval of 333-373 K to further study the nucleation and growth mechanism of silver in the urea-acetamide-LiBr. It should be noted that the surface of the working electrode must be re-polished before the next measurement to prevent any memory effect. Figure 2 displays typical current density-time transient curves, all exhibiting the classical shape characteristic of a nucleation process.

To determine the nucleation and growth mechanism of silver, the data from the chronoamperometric experiments are normalized to $(i/i_m)^2$ and (t/t_m) (i_m and t_m are the maximum current (mA) and the corresponding time (s) in the Faraday process), and then compared to the theoretical dimensionless $(i/i_m)^2$ *vs.* t/t_m curves proposed by Scharifker

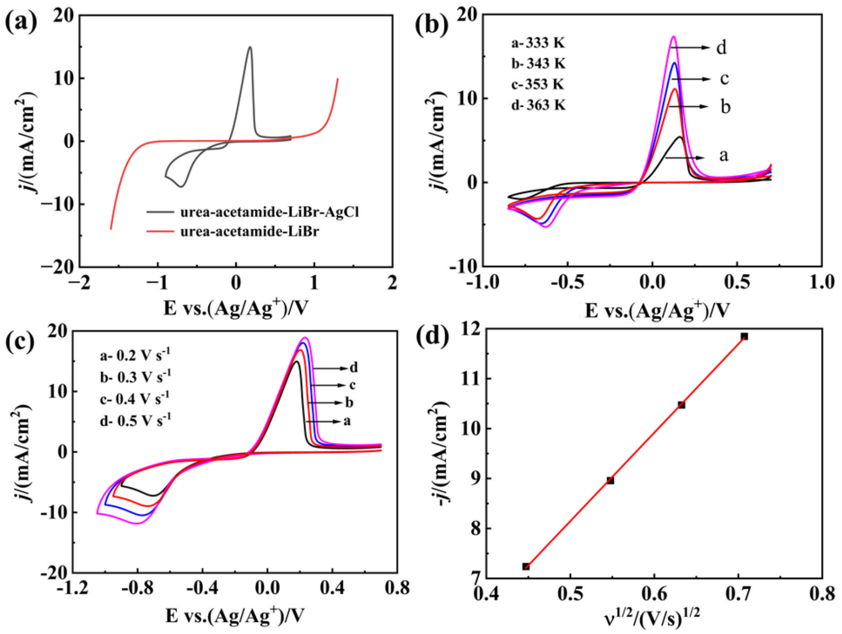

Figure 1. Cyclic voltammograms using a tungsten electrode in the (a) urea-acetamide-LiBr with and without AgCl (0.08 mol L^{-1}) at 353 K and 0.2 V s^{-1}; (b) urea-acetamide-LiBr-AgCl (0.08 mol L^{-1}) at different temperatures and 0.05 V s^{-1}; (c) urea-acetamide-LiBr-AgCl (0.08 mol L^{-1}) at 353 K under different scan rates; and (d) cathodic peak current densities of cyclic voltammogram using a tungsten electrode in urea-acetamide-LiBr-AgCl (0.08 mol L^{-1}) at 353 K under different scan rates.

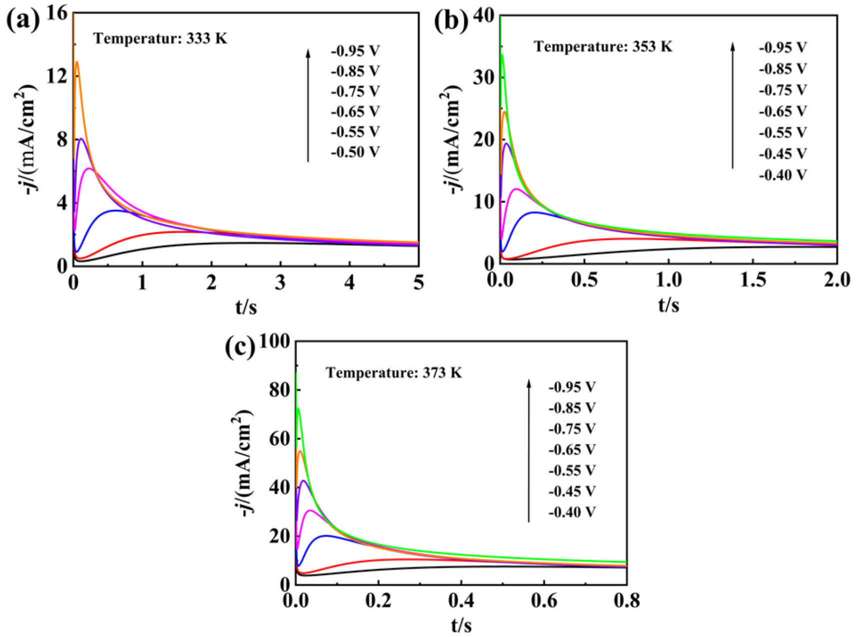

Figure 2. Current density-time transients of chronoamperometric experiments for urea-acetamide-LiBr-AgCl (0.08 mol L^{-1}) at different temperatures in the potential range from −0.40 to −0.95 V: (a) 333 K, (b) 353 K, and (c) 373 K.

for three-dimensional (3D) instantaneous (equation 3) and progressive (equation 4) nucleation processes:[25,26]

$$\left(\frac{i}{i_m}\right)^2 = 1.9542\left(\frac{t_m}{t}\right)\left(1-\exp\left[-1.2564\left(\frac{t}{t_m}\right)\right]\right)^2 \quad (3)$$

$$\left(\frac{i}{i_m}\right)^2 = 1.2254\left(\frac{t_m}{t}\right)\left(1-\exp\left[-2.3367\left(\frac{t}{t_m}\right)^2\right]\right)^2 \quad (4)$$

The experimental and theoretical plots of $(i/i_m)^2$ *vs.* t/t_m are shown in Figures 3-5. The plots deviated from the classical cases of instantaneous and progressive nucleation with diffusion-controlled growth theoretical models at lower temperatures and at a more positive potential, displaying an intermediate behavior controlled by a combination of diffusion and charge transfer process.[27] As the overpotential and temperature increase, the nucleation model tends to transition to instantaneous nucleation under diffusion control. This outcome arises because the charge transfer rate accelerates with the energy provided. Further analysis shows that the nucleation model of silver changes from a mixture process of instantaneous and progressive nucleation to instantaneous nucleation as the potential moves from –0.55 to –0.95 V at a temperature of 353 K. The nucleation model of silver is a mixture process of instantaneous and progressive nucleation with a tendency to change towards transient nucleation in the temperature range of 333-373 K at a potential of –0.65 V.

Figure 4b depicts a typical instantaneous nucleation process under diffusion control for the electrochemical reduction of Ag on a tungsten electrode within a potential range from –0.75 to –0.95 V at 353 K. The diffusion coefficient of Ag^I ions can be obtained from the maximum of current density-time transients for instantaneous nucleation via equation 5:[25,26]

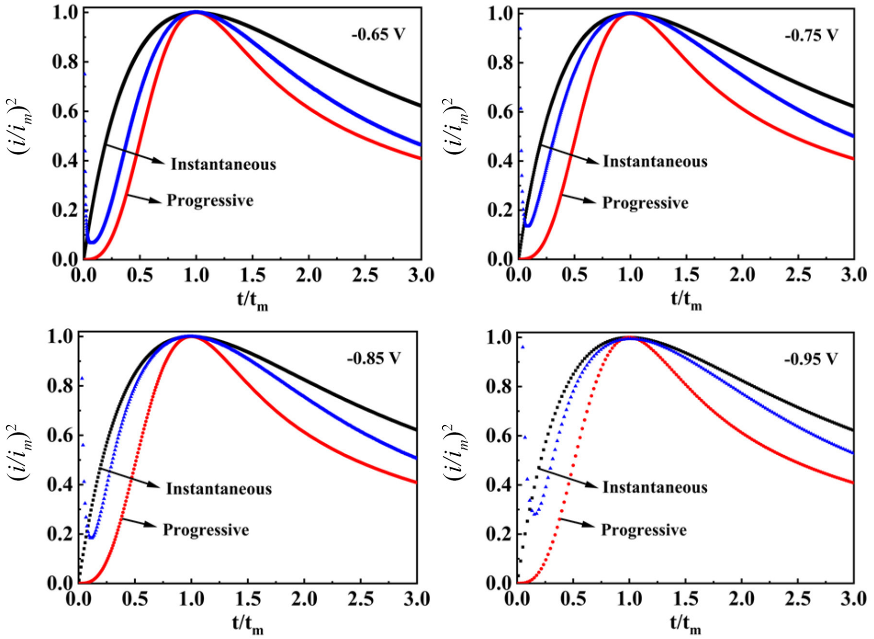

Figure 3. Comparison of the dimensionless current-time transients of chronoamperometric experiments for urea-acetamide-LiBr containing AgCl with the theoretical models of 3D nucleation process at different potentials and 353 K.

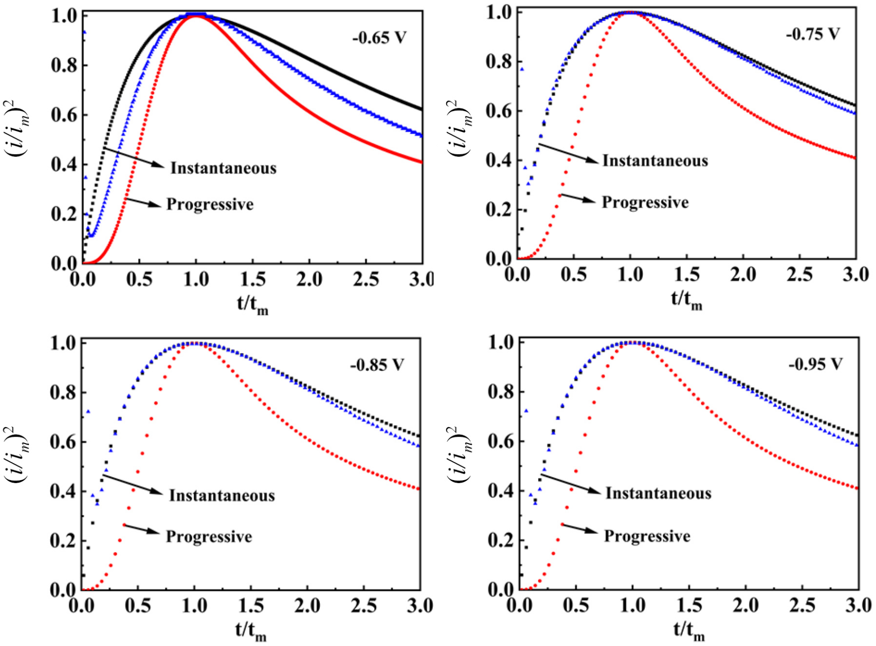

Figure 4. Comparison of the dimensionless current-time transients of chronoamperometric experiments for urea-acetamide-LiBr containing AgCl with the theoretical models of 3D nucleation process at different potentials and 353 K.

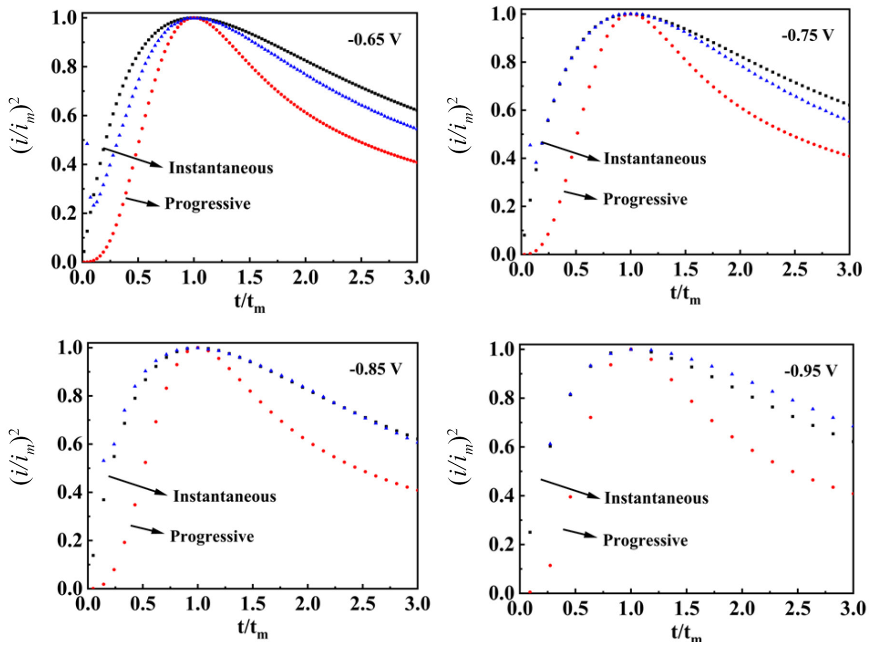

Figure 5. Comparison of the dimensionless current-time transients of chronoamperometric experiments for urea-acetamide-LiBr containing AgCl with the theoretical models of 3D nucleation process at different potentials and 373 K.

$$j_m^2 t_m = 0.1629(nFC)^2 D \quad (5)$$

where j_m is the maximum current density (A cm^{-1}); n is the number of transferred electrons; C is the bulk concentration of electroactive species (mol cm^{-3}); D is the diffusion coefficient of electro-active species (cm^2 s^{-1}). The average value of the diffusion coefficient of Ag^I was measured to be 1.39 × 10^{-6} cm^2 s^{-1}, in good agreement with the datum obtained from CV curves (1.38 × 10^{-6} cm^2 s^{-1}).

For instantaneous progress, the number density of nucleation (N) at different cathodic potentials can be calculated using equations 6 and 7:[25,26]

$$k = (8\pi CM / \rho)^{1/2} \quad (6)$$
$$j_m = 0.6382nFDC(kN)^{1/2} \quad (7)$$

where M and ρ are the molecular weight (107.87 g mol^{-1}) and density (10.49 g cm^{-3}) of the deposited silver, respectively. The value of k is calculated to be 0.1435, and the number densities of nucleation (N) of Ag^I at 353 K were obtained (Table 1).

All the slowly decaying current densities after t_m are ascribed to the increased diffusion layer thickness and overlap with others after a longer time. It presents a linear function between the decaying current density and $t^{-1/2}$, as described the Cottrell equation 8:[24]

$$j = nFD^{1/2}C(\pi t)^{-1/2} \quad (8)$$

Table 1. The values of the number density and diffusion coefficients of Ag^I at different potentials at 353 K

Potential / V	N / cm^{-2}	D / (cm^2 s^{-1})
−0.75	8.91 × 10^6	9.53 × 10^{-7}
−0.85	1.10 × 10^7	9.81 × 10^{-7}
−0.95	2.65 × 10^7	1.09 × 10^{-6}
	Average	1.01 × 10^{-6}

N: the number densities of nucleation; D: the diffusion coefficient of electro-active species.

where j is the current density (A cm^{-1}); t is the time. As shown in Figure 5, the plots of j *vs.* $t^{-1/2}$ give nearly straight lines. Based on equation 8 and the slopes of the straight lines of j *vs.* $t^{-1/2}$, the diffusion coefficients of Ag^I at different potentials at 353 K are listed in Table 1. The average value of the diffusion coefficients of Ag^I ions is calculated to be 1.01 × 10^{-6} cm^2 s^{-1} at 353 K, which is close to the value obtained from equation 5.

To confirm that the reduction process corresponded to the metallic silver deposition, the EDS analysis of the deposit obtained from urea-acetamide-LiBr on a copper substrate at −0.65 V and at 353 K shows that only elemental Ag can be detected at the electrode surface (Figure 6a), indicating the silver deposit with high-purity. XRD patterns (Figure 6b) clearly show several characteristic signals: the peaks located at 2θ 43.32°, 50.45°, 43.32°, 74.13°, and 89.94° are assigned to the crystalline copper (JCPDS No. 01-089-2838); the peaks located at 2θ 38.12°, 44.31°, 64.46°, 77.41°, and 81.56° are assigned to the crystalline silver (JCPDS No. 01-089-3722). No other peaks were observed. The above results indicate that high-purity

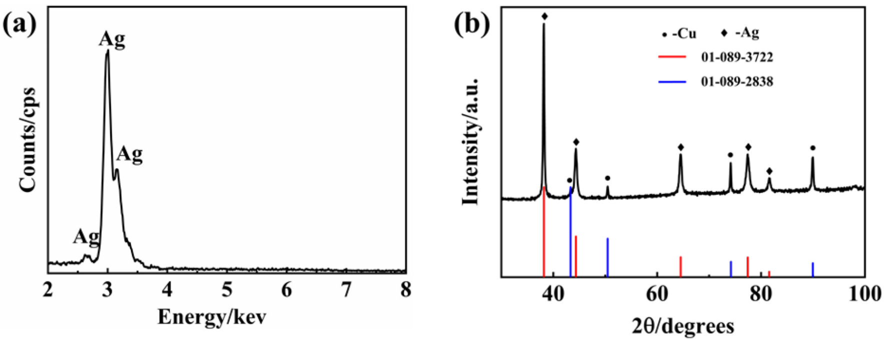

Figure 6. (a) EDS map and (b) XRD pattern of the silver electrodeposit obtained from urea-acetamide-LiBr on a copper substrate at –0.65 V and 353 K.

metallic silver films can be successfully prepared from the urea-acetamide-LiBr system.

The electrodeposition of silver was performed in the urea-acetamide-LiBr on copper substrates at different potentials (–0.55 to –0.70 V) and temperatures (333 to 363 K) for 2 h. The morphologies of the deposits obtained at the four different depositional conditions are shown in Figure 7. SEM images show that at –0.55 V and 353 K (Figure 7a), relatively uniform and dense deposits with some large particles are observed. At –0.60 V (Figure 7b), dendritic structures begin to appear. As the deposition potential negatively shifted to –0.65 V, the grain size of the deposits continued to grow, resulting in a loose and porous deposit with more dendrites (Figure 7c). At an even more negative potential of –0.70 V, larger dendritic deposits caused by the increased deposition rate at a more negative cathodic potential are observed (Figure 7d). The deposit is dense at 333 K and –0.65 V, as observed in Figure 7e. However, as the temperature increased to 343 K, grain size began to grow, resulting in small spherical nodular structures and dendritic structures appearing, as shown in Figure 7f. With a further increase of the temperature to 353 K, more porous, less uniform, and larger dendritic structures are formed (Figure 7c). At the even higher temperature of 363 K, dendritic deposits become more visible which was caused by the increased deposition rate at higher temperature (Figure 7g).

As indicated by the chronoamperometric results, the progressive nucleation predominates in the silver nucleation process at –0.55 V and 353 K. This process creates numerous nucleation sites for the growth of metallic silver, leading to a dense deposit with small grain sizes. At –0.70 V and 353 K, the nucleation model for silver shifts to instantaneous nucleation. This condition provides a limited number of nucleation sites, where metallic silver only grows on these sites, resulting in a porous deposit and dendrites easily generated. The morphology changes of silver deposits at the potential range from –0.55 to –0.70 V relative to the nucleation model change of silver from a mixture process of instantaneous and progressive nucleation to instantaneous nucleation. A similar phenomenon was observed in the silver deposition at –0.65 V as the temperature increased.

To study the SERS effect of silver films obtained in the urea-acetamide-LiBr molten salt, R6G was used as the probe molecule. A series of SERS spectra of R6G at different concentrations (10^{-11} to 10^{-4} mol L^{-1}, methanol solutions) were obtained to demonstrate the sensitivity of the Ag SERS substrates. The vibrational spectra of rhodamine R6G are shown in Figure 8a and Raman active modes are summarized in Table 2.[11,28] The R6G Raman spectra show the typical vibrational modes, with the higher intensity at 614 cm^{-1} (C–C in-plane bending in xanthene/phenyl rings), 775 cm^{-1} (C–H out-of-plane bending),

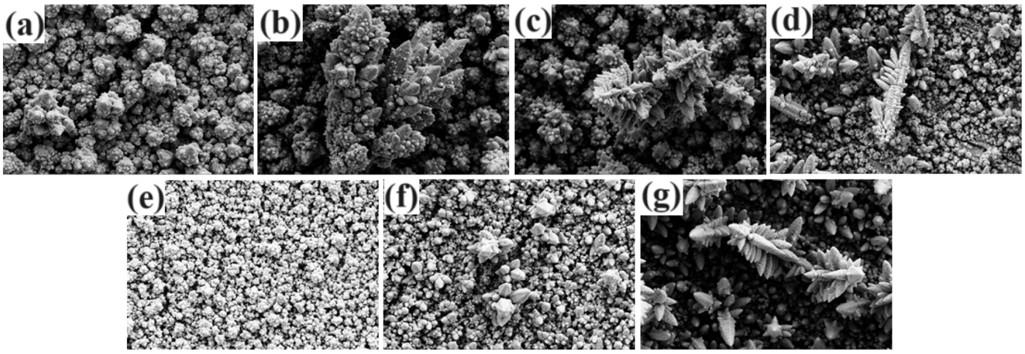

Figure 7. SEM micrographs of silver electrodeposit obtained in the urea-acetamide-LiBr: (a) –0.55 V, 353 K; (b) –0.60 V, 353 K; (c) –0.65 V, 353 K; (d) –0.70 V, 353 K; (e) –0.65 V, 333 K; (f) –0.65 V, 343 K; and (g) –0.65 V, 363 K.

Table 2. Assignment of vibrational modes in surface-enhanced Raman scattering (SERS) spectra of R6G dye obtained from Figure 8

Rh6G Raman shift / cm^{-1}	Assignment
614	C−C ring in-plane bending in xanthene/phenyl rings
775	C−H out-of-plane bending
1128	C−H in-plane bending in xanthene/phenyl rings
1185	C−H plane bending in xanthene ring
1274	C−O−C stretching in the $COOC_2H_5$ group on the phenyl ring
1321	hybrid mode (xanthene/phenyl rings and NHC_2H_5 group)
1366	C−C stretching in xanthene ring
1383	C−C stretching in xanthene ring
1441	C−N stretching in NHC_2H_5
1508	C−C strtching in xanthene ring
1576	C−C stretching in phenyl ring
1603	hybrid mode (phenyl ring with NHC_2H_5 group)
1651	C−C stretching in xanthene ring

1128 cm^{-1} (C−H in-plane bending in xanthene/phenyl rings), 1185 cm^{-1} (C−H in-plane bending in xanthene ring), 1321 cm^{-1} (hybrid mode concerning with NHC_2H_5 group and xanthene/phenyl rings), 1366 and 1508 cm^{-1} (both ascribed to C−C ring stretching related to the xanthene ring), 1576 cm^{-1} (C−C stretching related to the phenyl ring), and 1651 cm^{-1} (C−C stretching related to the xanthene ring). At lower R6G concentrations, the spectrum is slightly different, with some modes occurring at 1274 cm^{-1} (C−O−C stretching related to the $COOC_2H_5$ group bonded to the phenyl ring), and the 1603 cm^{-1} peak (related to C−H and C−C motion associated with the phenyl ring) was close to disappearing

From Figure 8a, the SERS spectral intensity decreases as the concentration decreases. The correlation between SERS intensity and R6G concentration is listed in Figure 8b. The SERS peak intensities of R6G at 614 cm^{-1} were set as the y-axis, and R6G concentration (logarithmic) was set as the x-axis, similar to the result in previous research.[29] Two linear regions exist in the whole concentration range. When the R6G concentration is in the range of 10^{-4} to 10^{-6} M, the linear regression equation is $y = 7724.63 \log(x) + 52390.41$, and the correlation coefficient is 0.9889 (n = 3). When the R6G concentration is in the range of 10^{-6} to 10^{-11} M, the linear regression equation is $y = 1063.78 \log(x) + 12050.07$, and the correlation coefficient is 0.9980 (n = 6). At a concentration as low as 10^{-11} mol L^{-1}, the Raman spectrum is slightly modified, but the modes ascribed to the C−C ring in-plane bending in xanthene/phenyl rings can be still detected. The R6G indicates that the proposed SERS substrates can trace extremely low-concentration analytes.

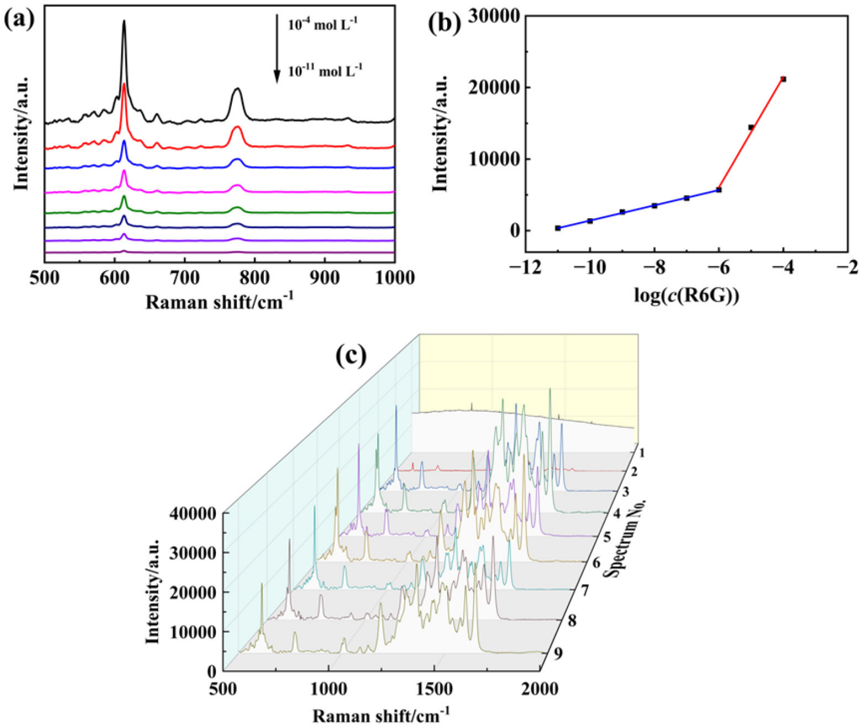

Figure 8. (a) SERS spectra of a series of R6G solutions with different concentrations from 10^{-3} to 10^{-9} M obtained from the Ag SERS active substrate; (b) piecewise linearity plots of R6G SERS intensity at 614 cm^{-1} *vs.* R6G solutions concentration in (a); and (c) representative Raman scattering spectra of a R6G assembled onto electrodeposited silver film obtained from urea-acetamide-LiBr at different cathodic potentials and temperatures: 1- R6G aqueous solution; 2- R6G on a polished silver substrate; 3- −0.55 V, 353 K; 4- −0.60 V, 353 K; 5- −0.65 V, 353 K; 6- −0.70 V, 353 K; 7- 333 K, −0.65 V; 8- 343 K, −0.65 V; 9- 363 K, −0.65 V.

Figure 8c shows the Raman spectra of R6G on the silver electrodeposits obtained at different cathodic potentials and different temperatures. The intensity at 1366 cm^{-1} of Raman signal for R6G aqueous solution (spectrum 1) and R6G on a polished silver substrate (spectrum 2) is measured to be 65.3 cps and 1.29×10^6 cps. Compared to that of a polished silver substrate, the silver deposits exhibit an excellent enhancement effect on Raman spectra (spectra 3-9).

The measured SERS intensities were compared to the intensity of normal Raman scattering to estimate the magnitude of the enhancement factor (EF) using the following equations 9-11:[30]

$$EF = (I_{\text{surf}}/N_{\text{surf}})/(I_{\text{bulk}}/N_{\text{bulk}}) \quad (9)$$
$$N_{\text{bulk}} = Ahc_{\text{bulk}}N_{\text{A}} \quad (10)$$
$$N_{\text{surf}} = (c_{\text{surf}}vAN_{\text{A}})/(\pi r)2 \quad (11)$$

where I_{surf} is the integrated intensity of R6G molecules absorbed on the portable SERS substrate (cps); I_{bulk} is the integrated intensity from R6G bulk solution (cps); N_{bulk} and N_{surf} are the numbers of R6G molecules in the bulk solution effectively illuminated by the laser beam and absorbed on the portable SERS substrate, respectively; A is the laser focal area (cm^2); c_{bulk} is the concentration of R6G bulk solution, 10^{-3} mol L^{-1}; N_{A} is the Avogadro constant, 6.02×10^{-23} mol^{-1}; h is the confocal depth, 1.3×10^{-3} cm; c_{surf} and v are the concentration (10^{-4} mol L^{-1}) and volume (10^{-5} L) of R6G solution used for SERS detection, respectively; r is the radius of 10^{-5} L R6G solution formed on the SERS substrate, 0.35 cm.

Among them, I_{SERS} and I_{bulk} were measured at 1366 cm^{-1}. The I_{surf} values were listed in Table 3. The enhancement factors calculated by the above equations for silver deposits are 10^7, which is at least 10^4-fold more sensitive than the polished silver substrate, indicating that the silver deposits obtained by the electrodeposition method have an excellent enhancement effect. The better deposition potential and temperature range are −0.55-0.70 V and 353-363 K.

It was found that the enhancement factor corresponding to spectrum 4 is the largest, while that of spectrum 7 is the smallest, the silver deposits were obtained at −0.60 V, 353 K, and −0.65 V, 343 K respectively. From the above analysis, it is clear that the nucleation model of silver is a mixture of instantaneous and progressive nucleation at −0.60 V, 353 K resulting in porous deposits with dendrites, and the progressive nucleation is dominant in the nucleation process of silver at −0.55 V and 353 K resulting in relatively uniform and dense deposits. The combination of chronoamperometric experiments and morphological analysis of deposits, the value change of enhancement factor indicated that higher enhancement factors are more easily obtained for silver deposits prepared by electrodeposition controlled by instantaneous nucleation, especially in the mixed nucleation mode. In future work, how precisely controlling the silver electrodeposition process by optimizing the experimental conditions (such as the deposition time, potential, and temperature) to obtain higher enhancement factors becomes even more important.

Conclusions

Electrochemical behaviors and electrodeposition of silver were investigated in the urea-acetamide-LiBr mixture. Chronoamperometric experiments presented that the nucleation of silver is controlled by a combination of diffusion and charge transfer process at positive potential and lower temperature, and turns to instantaneous nucleation under diffusion control with increasing overpotential and temperature. The electrochemical deposition of silver was successfully performed at various potentials (−0.55 to −0.70 V *vs.* Ag/Ag$^+$) and temperatures (333 to 363 K). The SEM images indicated that better depositions can be obtained at less negative cathodic potential and lower temperatures. Pure silver deposits are verified by EDS and XRD. Rhodamine 6G was used as probe molecules for SERS experiments, showing that those new active substrates have high sensitivity to SERS response with high enhancement factors of approximately

Table 3. The enhancement factors of silver films prepared at different conditions

Spectrum No.	Substrate	Condition	I_{surf}	$I_{\text{surf}}/I_{\text{bulk}}$	EF
2	bulk silver plate	polished	1.29×10^6	1.98×10^4	9.88×10^3
3	silver electrodeposit	−0.55 V, 353 K	5.41×10^9	8.28×10^7	4.14×10^7
4		−0.60 V, 353 K	8.70×10^9	1.33×10^8	6.66×10^7
5		−0.65 V, 353 K	4.95×10^9	7.58×10^7	3.79×10^7
6		−0.70 V, 353 K	6.99×10^9	1.07×10^8	5.35×10^7
7		−0.65 V, 333 K	3.29×10^9	5.04×10^7	2.52×10^7
8		−0.65 V, 343 K	4.19×10^9	6.42×10^7	3.21×10^7
9		−0.65 V, 363 K	5.48×10^9	8.39×10^7	4.20×10^7

I_{sur}: the integrated intensity of R6G molecules absorbed on the portable SERS substrate; I_{surf}: integrated intensity of R6G molecules absorbed on the portable SERS substrate; I_{bulk}: integrated intensity from R6G bulk solution; EF: enhancement factor.

10^7 and allow Raman scattering also for diluted solutions (10^{-11} mol L^{-1}). In future work, how precisely controlling the silver electrodeposition process by optimizing the experimental conditions (such as the deposition time, potential, and temperature) to obtain higher enhancement factors becomes even more important.

Acknowledgments

This work was financially supported by the Henan Province Housing and Urban-Rural Construction Science and Technology Program (K-2317), doctoral research start-up funds from Henan Urban Construction College (K-Q2022014 and K-Q2022015), Henan Provincial Science and Technology Research Project (222102240055), and open fund of the State Key Laboratory of Advanced Metallurgy (K23-05).

Author Contributions

Chengyuan Liu was responsible for conceptualization, investigation, writing original draft, and funding acquisition; Chaoyang Jie and Dao Cao for methodology and investigation (electrochemical analysis); Yu Liu and Shuning Gao for methodology and investigation (XRD, SEM, and Raman analysis); Fengcui Li for project administration and writing review and editing. All authors have read the final manuscript and approved the submission.

References

1. Guo, J. C.; Zeng, F. Y.; Guo, J. H.; Ma, X.; *J. Mater. Sci. Tech.* **2020**, *37*, 96. [Crossref]
2. Zhang, J.; Ma, X.; Wang, Z.; *Talanta* **2019**, *195*, 8. [Crossref]
3. Mercadal, P. A.; Encina, E. R.; Villa, J. E. L.; Coronado, E. A.; *J. Phys. Chem. C* **2021**, *125*, 4056. [Crossref]
4. Hardy, M.; Oppenheimer, P. G.; *Nanoscale* **2024**, *16*, 3293. [Crossref]
5. Shi, L.; Zhang, L. M.; Tian, Y.; *Anal. Sens. **2023***, *3*, e202200064. [Crossref]
6. Dey, P.; *ACS Meas. Sci. Au* **2023**, *3*, 434. [Crossref]
7. Mazur, N. V.; Kapush, O. A.; Isaieva, O. F.; Budzulyak, S. I.; Buziashvili, A. Y.; Pirko, Y. V.; Skoryk, M. A.; Yemets, A. I.; Hreshchuk, O. M.; Yukhymchuk, V. O.; Dzhagan, V. M.; *Phys. Chem. Solid State* **2023**, *24*, 682. [Crossref]
8. Luo, X.; Pan, R.; Cai, M. Y.; Liu, W. J.; Chen, C. H.; Jiang, G. C.; Hu, X. Y.; Zhang, H. J.; Zhong, M. L.; *Sensor Actuators, B* **2021**, *326*, 128826. [Crossref]
9. Dzhagan, V.; Mazur, N.; Kapush, O.; Skoryk, M.; Pirko, Y.; Yemets, A.; Dzhahan, V.; Shepeliavyi, P.; Valakh, M.; Yukhymchuk, V.; *ACS Omega* **2024**, *9*, 4819. [Crossref]
10. Coluccio, M. L.; Das, G.; Mecarini, F.; Gentile, F.; Pujia, A.; Bava, L.; Tallerico, R.; Candeloro, P.; Liberale, C.; Angelis, F. D.; Fabrizio, E. D.; *Microelectron. Eng.* **2009**, *86*, 1085. [Crossref]
11. Virga, A.; Rivolo, P.; Frascella, F.; Angelini, A.; Descrovi, E.; Geobaldo, F.; Giorgis, F.; *J. Phys. Chem. C* **2013**, *117*, 20139. [Crossref]
12. Yu, J.; Wu, J. G.; Yang, H.; Li, P.; Liu, J.; Wang, M.; Pang, J. H.; Li, C. B.; Yang, C.; Xu, K. C.; *ACS Appl. Mater. Interfaces* **2022**, *14*, 43877. [Crossref]
13. He, L.; Rodda, T.; Haynes, C.; Deschaines, T.; Strother, T.; Francisco Diez-Gonzalez, F.; Labuza, T. P.; *Anal. Chem.* **2011**, *83*, 1510. [Crossref]
14. Luo, H. R.; Huang, Y. Q.; Lai, K. Q.; Rasco, B. A.; Fan, Y. X.; *Food Control* **2016**, *68*, 229. [Crossref]
15. Ibañez, D.; Fernández, B. C.; Heras, A.; Colina, A.; *J. Phys. Chem. C* **2014**, *118*, 23426. [Crossref]
16. Rivera, R. R. D.; Navarro, S. M. E.; Arizmendi, M. A.; Sanchez, D. M.; *Nanotechnology* **2020**, *31*, 465605. [Crossref]
17. Xia, Y.; Wu, Y.; Hang, T.; Chang, J. M.; Li, M.; *Langmuir* **2016**, *32*, 3385. [Crossref]
18. Liu, P.; Du, Y. P.; Yang, Q. Q.; Tong, Y. X.; Hope, G. A.; *J. Electrochem. Soc.* **2006**, *153*, C57. [Crossref]
19. Abbott, A. P., Capper, G.; Davies, D. L.; Rasheed, R. K.; *Chem. Eur. J.* **2004**, *10*, 3769. [Crossref]
20. Liu, P.; Du, Y. P.; Yang, Q. Q.; Li, G. R.; Tong, Y. X.; *Electrochim. Acta* **2006**, *52*, 710. [Crossref]
21. Wang, S. L.; Lin, J. B.; Cai, Q. Y.; Zhang, Y.; *J. Alloys Compd.* **2008**, *450*, 142. [Crossref]
22. Li, J. X.; Lai, H.; Fan, B. Q.; Zhuang, B.; Guan, L. H.; Huang, Z. G.; *J. Alloys Compd.* **2009**, *477*, 547. [Crossref]
23. Margarita, M. H.; Ignacio, G. L.; *J. Electrochem. Soc.* **2004**, *151*, C220. [Crossref]
24. Bard, A. J.; Faulkner, R. L.; *Electrochemical Methods Fundamentals and Applications*; John Wiley & Sons: New York, 2001, ch. 2.
25. Gunawardena, G.; Hills, G.; Montenegro, I.; Scharifker, B.; *J. Electroanal. Chem.* **1982**, *138*, 225. [Crossref]
26. Scharifker, B.; Hills, G.; *Electrochim Acta* **1983**, *28*, 879. [Crossref]
27. Cao, Y.; West, A. C.; *J. Electrochem. Soc.* **2002**, *149*, C223. [Crossref]
28. Watanabe H., Hayazawa N., Inouye, Y., Kawata, S.; *J. Phys. Chem. B* **2005**, *109*, 5012. [Crossref]
29. Chen, J.; Shen, W.; Das, B.; Li, Y.; Qin, G.; *RSC Adv.* **2014**, *4*, 22660. [Crossref]
30. Yu, H. Z.; Zhang, J.; Zhang, H. L.; Liu, Z. F.; *Langmuir* **1999**, *15*, 16. [Crossref]

Submitted: March 14, 2024